Unraveling the hydrogen sulfide aging mechanism on electrical-thermal–mechanical property degradation of sintered nanocopper interconnects used in power electronics packaging

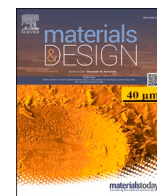Chen, Wei; Liu, Xu ; Hu, Dong; Liu, Xu; Zhu, Xi; Fan, Xuejun; Zhang, Guoqi; Fan, Jiajie

Important note
To cite this publication, please use the final published version (if applicable).
Please check the document version above.

Unraveling the hydrogen sulfide aging mechanism on electrical-thermal–mechanical property degradation of sintered nanocopper interconnects used in power electronics packaging

Wei Chen [a], Xu Liu [a], Dong Hu [b], Xu Liu [b], Xi Zhu [a,c], Xuejun Fan [d], Guoqi Zhang [b], Jiajie Fan [a,b,c,*]

[a] Institute of Future Lighting, Academy for Engineering & Technology, Shanghai Engineering Technology Research Center for SiC Power Device, Fudan University, Shanghai 200433, China
[b] EEMCS Faculty, Delft University of Technology, Delft 2628, the Netherlands
[c] Research Institute of Fudan University in Ningbo, Ningbo 315336, China
[d] Department of Mechanical Engineering, Lamar University, PO Box 10028, Beaumont, TX 77710, USA

ARTICLE INFO

ABSTRACT

During operation in environments containing hydrogen sulfide (H₂S), such as in offshore and coastal environments, sintered nanoCu in power electronics is susceptible to degradation caused by corrosion. In this study, experimental and molecular dynamics (MD) simulation analyses were conducted to investigate the evolution and mechanism of H₂S-induced corrosion of sintered nanoCu, and bulk Cu was used as the reference. The following results are obtained: (1) Both sintered nanoCu and bulk Cu reacted with O_2 prior to reacting with H_2S, forming Cu_2O, Cu_2S, CuO, and CuS. In addition, sintered nanoCu exhibited more severe corrosion. (2) For both sintered nanoCu and bulk Cu, H_2S-induced corrosion resulted in the deterioration of electrical, thermal, and mechanical properties, and sintered nanoCu experienced a greater extent of deterioration. (3) As was ascertained through Reactive Force Field (ReaxFF) MD simulations, the penetration of H_2S and O_2 combined with the upward migration of Cu resulted in the formation of a corrosion film. In addition, compared to bulk Cu, the H_2S and O_2 penetration in the sintered nanoCu structure was observed to occur to a greater depth, accounting for the more pronounced performance degradation.

1. Introduction

Power electronics, utilizing wide-bandgap (WBG) semiconductor materials such as silicon carbide (SiC) and gallium nitride (GaN), offer significant advantages such as high-temperature resistance and high energy efficiency [1–3]. Owing to its remarkable electrical, thermal, and mechanical properties, Cu is widely employed in semiconductor packaging [4–6]. In power electronics with WBG semiconductor materials, Cu has been used in various applications, including as a foundational baseplate, leadframe, wire-bonding material, and direct copper bonding substrate (DBC) [7–11]. Furthermore, traditional tin-based solder, with its low melting point, cannot meet the high-temperature durability needs of WBG semiconductor materials [12,13]. As a result, sintered nanoCu has the potential to become the high-temperature die attachment material for WBG semiconductors [14–16].

Power electronics operating in natural environments are vulnerable to corrosion owing to various factors, including ambient humidity, oxygen, and corrosive gases [17–20]. This is particularly pronounced in severe environmental settings such as in coastal and offshore areas characterized by elevated concentrations of hydrogen sulfide (H₂S) [21,22]. In addition, power electronics deployed in industrial facilities such as mines, paper mills, wastewater/waste treatment plants, farms, and fertilizer plants are exposed to elevated pollutant levels [23,24], thereby intensifying the corrosion challenges. Corrosive gases such as H₂S can enter the power electronics by permeating through the encapsulation silicone and the interface between the silicone and the case and can subsequently chemically react with the materials of various packaging components [25,26]. The formation of a stable surface passivation layer for Cu is inherently challenging, rendering Cu highly susceptible to ongoing corrosion.

Some studies have reported corrosion and electrochemical migration phenomena in bulk Cu used in electronics packaging [27–33]. Becker et al. [27] conducted H_2S-aging tests on bulk Cu plates and observed the localized distribution of Cu_2S on the copper surface. Tran et al. [28] reported that under high temperature and humidity conditions and in the presence of H_2S, bulk Cu predominantly forms Cu_2O and Cu_2S initially, followed by the formation of CuO. The reaction rate was accelerated by increasing temperature, humidity, and H_2S concentration, as assessed using a coulometric method. Yu et al. [29] found that during their examination of the failure mechanisms in a bulk Cu wire bonding on an Al layer formed by metallization in an NaCl solution, Cl^- penetrated cracks in the Cu–Al bonding interface, causing the failure of the wire bonding. Xu et al. [30] demonstrated that Ca^{2+} in the liquid could inhibit the corrosion of bulk Cu. During operational conditions, various bulk Cu components within power devices have the potential to be in a voltage-biased state. Consequently, some studies have focused on the electrochemical migration of bulk Cu under biased conditions [31–33]. Bayer et al. [31] observed dendritic growth between two bulk Cu electrodes bonded on an Al_2O_3 plate in deionized water, tap water, a hydrochloric acid solution (HCl), and a sulfuric acid solution (H_2SO_4), under a 4 V bias. The dendritic growth direction extended from the cathode toward the anode. Wassermann et al. [32] observed dendritic growth in the same direction under a high humidity, high voltage, and H_2S-containing atmosphere. Increased humidity, voltage, and H_2S concentration (not exceeding 30 ppm) all promote the migration of Cu. Tan et al. [33] reported the dendritic growth between two bulk Cu electrodes in air atmosphere. They proposed that the tape between the electrodes absorbed moisture from the air, thereby serving as an electrolyte.

Only a few studies have focused on the corrosion and electrochemical migration phenomena in sintered nanoCu [22,34]. Wang et al. [22] compared the corrosion behavior of sintered nanoCu and sintered Ag exposed to 100 ppb H_2S for 168 h, with sintered nanoCu exhibiting superior corrosion resistance under thermal shock. However, they did not investigate the temporal evolution of corrosion. Lee et al. [34] utilized intensive pulsed light (IPL) sintering to fabricate sintered nanoCu electrodes and examined their electrochemical migration behavior in water by applying biases ranging from 3 V to 9 V. They observed the dendritic growth extending from the cathode to the neighboring anode and noted that increasing voltage could shorten the time to dendrite short-circuiting.

The observation of microscopic molecular/atomic changes during the corrosion process through experiments is challenging. However, molecular dynamics (MD) simulations that model the interactions and movements of molecules or atoms within a system by using accurate potential functions and boundary conditions offer valuable insights into the process and mechanisms of metal corrosion. Consequently, MD simulations have significant potential for the analysis of extensive and complex Cu corrosion [35]. Numerous studies have documented the corrosion behavior of bulk Cu in both atmospheric and liquid environments, along with proposed protective measures [36–39]. However, few studies have focused on elucidating the corrosion behavior of sintered nanoCu.

Generally, as shown in Fig. 1, environmental corrosion stressors can lead to significant deterioration of Cu materials within electronics, creating vulnerable points of failure within electronic packages. The degradation is typically categorized on the basis of the corrosion and dendritic growth [23]. However, a comprehensive understanding of time-dependent corrosion evolution and mechanism in sintered nanoCu is lacking, and insight into the mechanisms of sintered nanoCu corrosion gained through simulations has also been limited.

In this study, sintered and bulk Cu samples were exposed to a 336-h aging process using 1 ppm H_2S. The morphologies and performances were assessed at 24-h intervals. Subsequently, the mechanisms of H_2S and O_2 penetration into the sintered and bulk Cu samples were analyzed through MD simulations. The rest of this manuscript is organized as follows: Section 2 presents the sample preparation, experimental setup, and characterization methodology. Section 3 analyzes the corrosion behavior and relevant chemical reaction. Section 4 examines the influence of H_2S-induced corrosion on thermal, electrical and mechanical performances. Section 5 compares the mechanisms of H_2S penetration into the sintered and bulk Cu samples. Finally, Section 6 presents the conclusions of the study.

2. Experimental details

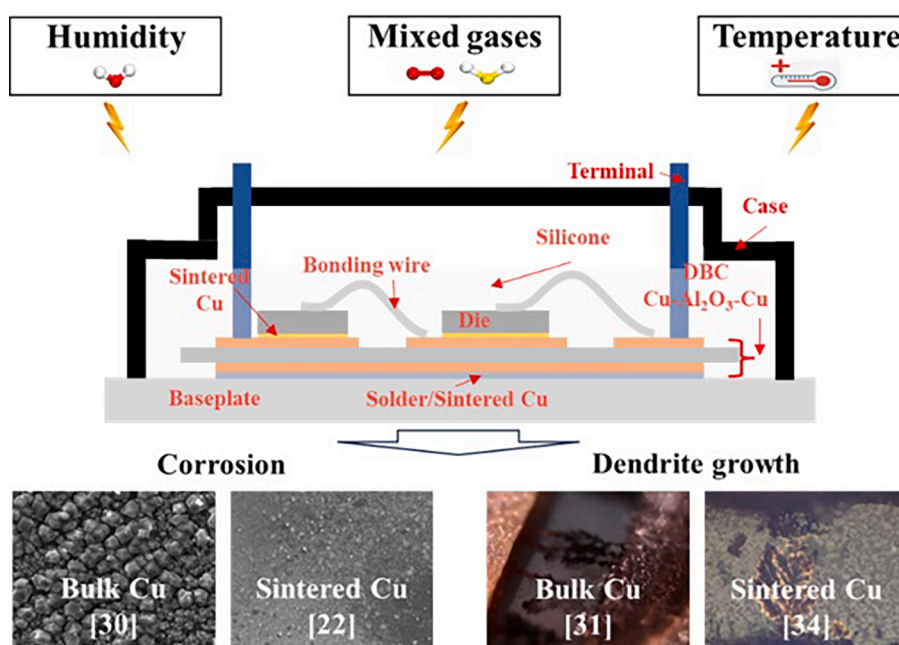This section presents the details about sample preparation, experimental setup, and characterization methodologies.

Fig. 1. Schematic representation of power module failure in an H_2S-enriched environment.

2.1. Sample preparation

To investigate the corrosion process involving H₂S, two types of samples, i.e., the sintered and bulk Cu samples, were employed in this study, both with dimensions of 5 mm × 5 mm × 1 mm. The Cu nanoparticle paste used in this study was composed of Cu nanoparticles with an average particle size of about 150–300 nm, along with ethylene glycol (99.5 %, from Aladdin Reagent Co., Ltd.) and terpinol (95.0 %, from Aladdin Reagent Co., Ltd.) [14]. To obtain the sintered nanoCu samples, a square-shaped mold was designed, as shown in Fig. 2(a). Initially, the Cu nanoparticle paste was injected into the mold, followed by preheating of the paste at 120 °C for 30 min in a vacuum oven (DZF-6012, YIHENG). Subsequently, pressure-assisted sintering was conducted in a nitrogen atmosphere using an industrial standard sintering machine (Sinterstar Innovate-F-XL, Boschman) at a temperature of 250 °C and a pressure of 20 MPa for 25 min. The sintering temperature and pressure profiles and the sintering machine are depicted in Fig. 2 (b). Bulk Cu samples were purchased from a commercial company (SHENG SHI JING New Material Co., Ltd, China). The sintered and bulk Cu samples are shown in Fig. 2(c).

To explore the impact of H₂S on the die attachment structure, this study employed two types of samples, namely the dummy die joint and the SiC die joint. First, the paste was stencil printed onto DBC substrates, and the dimensions of the printed paste were 8 mm × 8 mm × 0.15 mm. Subsequently, the dummy die with dimensions of 3 mm × 3 mm × 1 mm or the SiC die (S4601M) with dimensions of 5 mm × 5 mm × 0.15 mm was placed on the printed paste. Like the sintered nanoCu samples, the joint samples were also subjected to the same processes of preheating and pressure-assisted sintering. The dummy die material was a Cu block coated with a layer of silver. The dummy die joint and SiC die joint samples are shown in Fig. 2(d).

2.2. Experimental setup

To investigate the corrosion induced by H₂S, the sintered nanoCu, bulk Cu, dummy die joint, and SiC die joint samples were aged in a H₂S gas atmosphere using a commercial gas corrosion test chamber (GH-180, YAMASAKI) for 336 h. During the aging process, the temperature, relative humidity, and H₂S concentration were set to 45 °C, 85 %, and 1 ppm, respectively. Before H₂S aging, the surfaces of all sintered and bulk Cu samples were polished. Nine sintered nanoCu samples and nine bulk Cu samples were taken out every day, and all the joint samples were retrieved upon completion of the aging process.

2.3. Characterization methodologies

Scanning electron microscopy with energy-dispersive X-ray spectroscopy (SEM/EDS; SU8010, Hitachi) was used to detect the microstructure and elemental composition of the sample surfaces. To determine the thickness of the corrosion layer, cross-sectional cuts and analysis were performed on the sintered samples using a focused-ion-beam scanning electron microscope (FIB-SEM; Crossbeam 550, ZEISS). Subsequently, to further determine the composition of the corrosion products in the aged samples, X-ray diffraction (XRD; D8, Bruker) with Cu Kα radiation (λ = 0.15418 nm) was employed. X-ray photoelectron spectroscopy (XPS) (Axis Supra+, Shimadzu) equipped with an Al Kα excitation source (hv = 1486.6 eV) was used to analyze the chemical states of the elements in the corrosion products. The four-probe method was employed to measure the electrical resistivity of the samples using a four-probe tester (RTS-11, 4probes TECH). The thermal conductivity was determined using a flash apparatus (LFA457, Netzsch). The thermal deformation property was assessed using a thermomechanical analyzer (TMA/SDTA 2+, Mettler-Toledo). The surface mechanical properties of the samples were tested and compared using a nanoindentation testing system (iNano, KLA). The shear strength of the sintered nanoCu joint was measured using a shear tester (Dage4000, Nordan).

3. Corrosion process analysis

In this section, the morphological evolution of the sintered and bulk Cu samples during H₂S-aging is discussed. The corrosion products are assessed and the potential reactions involved are analyzed.

3.1. Morphological characterization

The surface of the sintered and bulk Cu samples was inspected using SEM before and after aging, and the results are shown in Fig. 3. The surface of the sintered nanoCu sample showed an increase in the amount
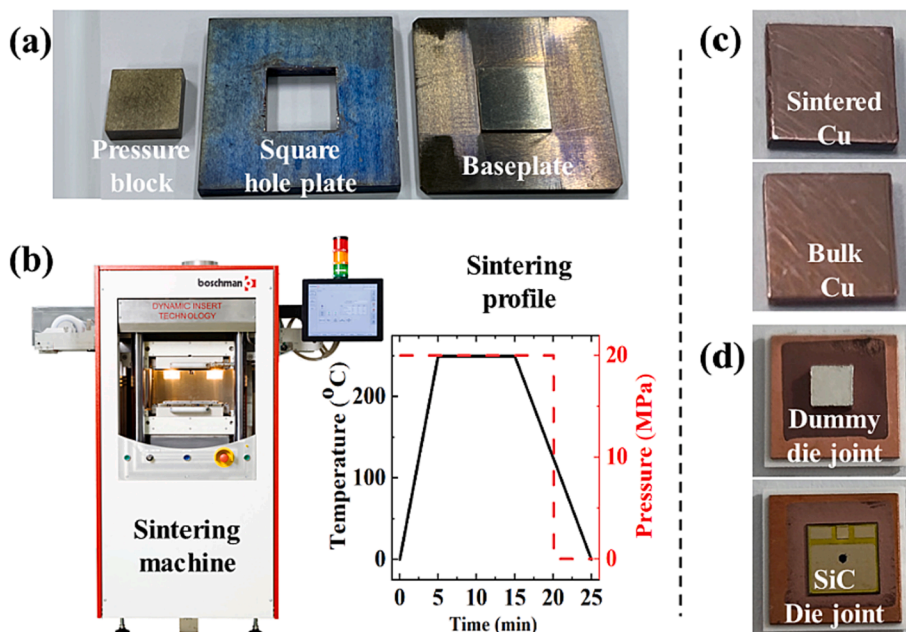

Fig. 2. (a) Designed mold. (b) Sintering temperature and pressure profiles and sintering machine. (c) Sintered and bulk Cu samples. (d) Dummy die joint and SiC die joint samples.
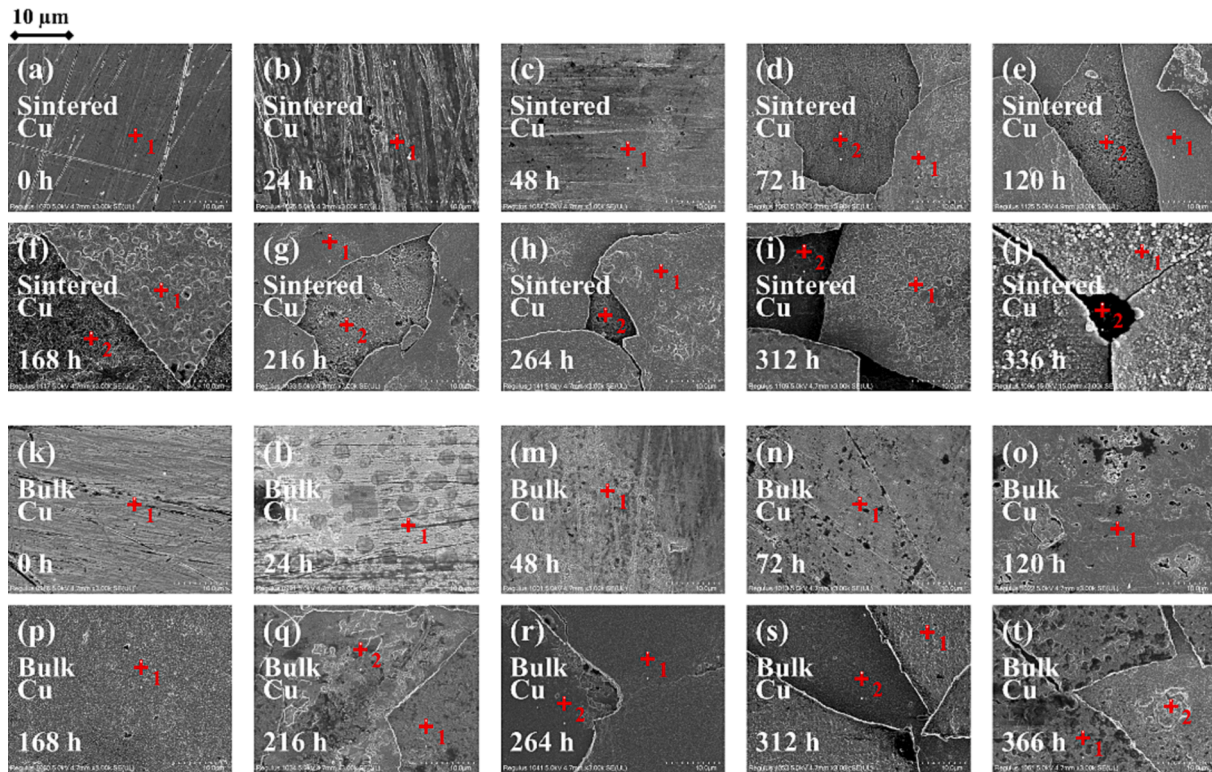
Fig. 3. Evolution of surface morphology with increasing aging time for sintered and bulk Cu samples. Panels (a)–(j) represent the sintered nanoCu samples at aging times of 0 h, 24 h, 48 h, 72 h, 120 h, 168 h, 216 h, 264 h, 312 h, and 336 h, respectively. Panels (k)–(t) correspond to the bulk Cu samples at aging times of 0 h, 24 h, 48 h, 72 h, 120 h, 168 h, 216 h, 264 h, 312 h, and 336 h, respectively. The upper layer region of the corrosion film was designated as "region 1", and the exposed region after corrosion film detachment was designated as "region 2".

of corrosion products as the aging time increased. After 48 h of aging, the sample surfaces became completely covered by a film of corrosion products, as depicted in Fig. 3(c). As the volume of the corrosion products increased, the accumulated compressive stress caused the localized separation of the corrosion product film from the sintered copper substrate. As shown in Fig. 3(d), after 72 h of aging, the separated corrosion product film experienced fracture, subsequently detaching from the sample surface. During the H_2S aging process, the bulk Cu sample showed a surface morphology evolution similar to that of the sintered nanoCu sample. However, as shown in Fig. 3 (q), fractures and detachment of the corrosion product film of the bulk Cu sample were observed after 216 h of aging, which indicated that the sintered nanoCu sample underwent more severe corrosion. Similar phenomena of fractures and detachment during the H_2S aging process have been previously reported for Cu [27,40,41].

To further understand the surface morphological evolution during H_2S aging, elemental analysis was conducted on sintered and bulk Cu samples using EDS. Fig. 4 visually depicts the elemental O and S contents

in the upper layer (identified as region 1) and in the exposed part after detachment (identified as region 2). Throughout the entire corrosion stage, the elemental O and S contents in the upper layer exhibited a trend of initial increase, followed by stabilization. However, in the initial 48 h aging process for the sintered nanoCu sample, the increase in the S content in the upper layer occurred after the increase in the O content. Further, in the subsequent 72 h to 120 h aging period, within the exposed part, the O content remained consistently higher, while the S content remained notably low, increasing at a slower rate. Therefore, during H_2S aging, Cu exhibited a greater propensity to react with O_2 prior to reacting with H_2S. Next, the dynamic variation in the O and S contents in the exposed part after 72 h of aging might be attributed to the fracture and detachment of the initial corrosion layer that subsequently exposed the underlying layers to H_2S and O_2 and thus led to the formation of additional corrosion products. The bulk Cu sample exhibited similar changes in the O and S contents. However, the O and S contents in the bulk Cu sample were slightly lower than those in the sintered nanoCu sample.
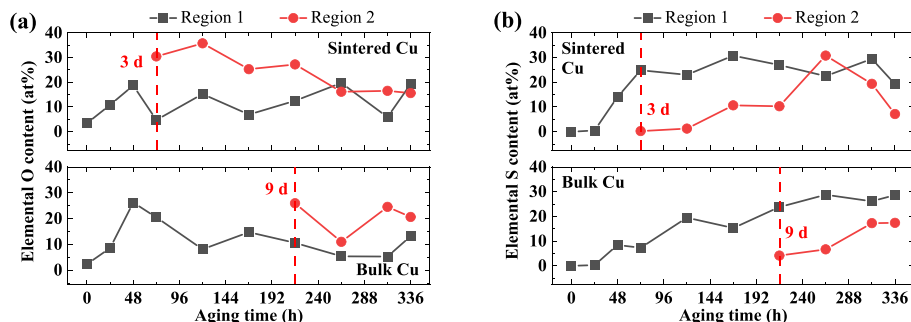

Fig. 4. Evolution of O and S contents on the surface of aged samples over aging time: (a) elemental O content and (b) elemental S content.

Cross-sections measuring approximately 12 μm × 12 μm were obtained using FIB, from the central part of the surfaces of sintered and bulk Cu samples subjected to 336 h of H₂S aging. Prior to FIB processing, platinum spraying of the target areas was conducted. The results of FIB-SEM/EDS analysis are presented in Fig. 5. The corrosion product layer was composed of Cu, O, and S elements. The average calculations of 3 typical thickness values revealed that the thicknesses of corrosion product layers for the sintered and bulk Cu samples were approximately 1.35 μm and 1.16 μm, respectively. For both sintered and bulk Cu samples, a distinct interface existed between the corrosion product layer and Cu matrix.

3.2. Analysis of corrosion product

To identify the composition of corrosion products, XRD and XPS analyses were conducted on both sintered and bulk Cu samples before and after 336 h of aging. The detection capabilities of XPS and XRD extend to surface and interior analyses of corrosion product films, probing depths in the range of several nanometers and tens of micrometers, respectively. The XRD results of both sintered and bulk Cu samples are shown in Fig. 6. As depicted in Fig. 6(a), after 336 h of H₂S aging, a crystalline layer of Cu₂O (PDF#99–0041) emerged on the surface of the sintered nanoCu sample. In contrast, the unaged sintered

nanoCu sample exhibited only metallic Cu (PDF#85–1326). Further, on the bulk Cu sample, Cu₂O crystals were also formed during the H₂S aging process. However, the amount of generated Cu₂O in the bulk Cu sample was much lower than that in the sintered nanoCu sample, as shown in Fig. 6(b). Both sintered and bulk Cu samples did not exhibit the presence of S after aging, possibly due to the formation of amorphous S compounds with Cu.

XPS analysis was also utilized to study the corrosion products present in the corroded samples conducted in Thermo Scientific™ Avantage. Fig. 7 shows the XPS spectra of both the sintered and bulk Cu samples. As shown in Fig. 7(a), the surfaces of the sintered nanoCu samples, both before and after aging, showed the presence of O, Cu, and C elements. However, S was found only in the aged sintered nanoCu samples. As depicted in Fig. 7(b), both the unaged and 336-h-aged sintered nanoCu samples exhibited a peak at 932.3 eV, indicating the presence of metallic Cu [42]. Furthermore, the spectrum of the 336-h-aged sintered nanoCu sample showed an additional peak at 934.4 eV, indicating the formation of CuO [43,44]. The presence of a satellite peak and its corresponding initiation and termination positions further substantiated the existence of CuO. As depicted in Fig. 7(c), the unaged sintered nanoCu sample did not exhibit any traces of S. However, in the 336-h-aged sintered nanoCu sample, the peaks observed at 162.9 eV for Cu⁺-S 2p1/2 and at 161.7 eV for Cu⁺-S 2p3/2 provided clear confirmation of the presence of Cu₂S
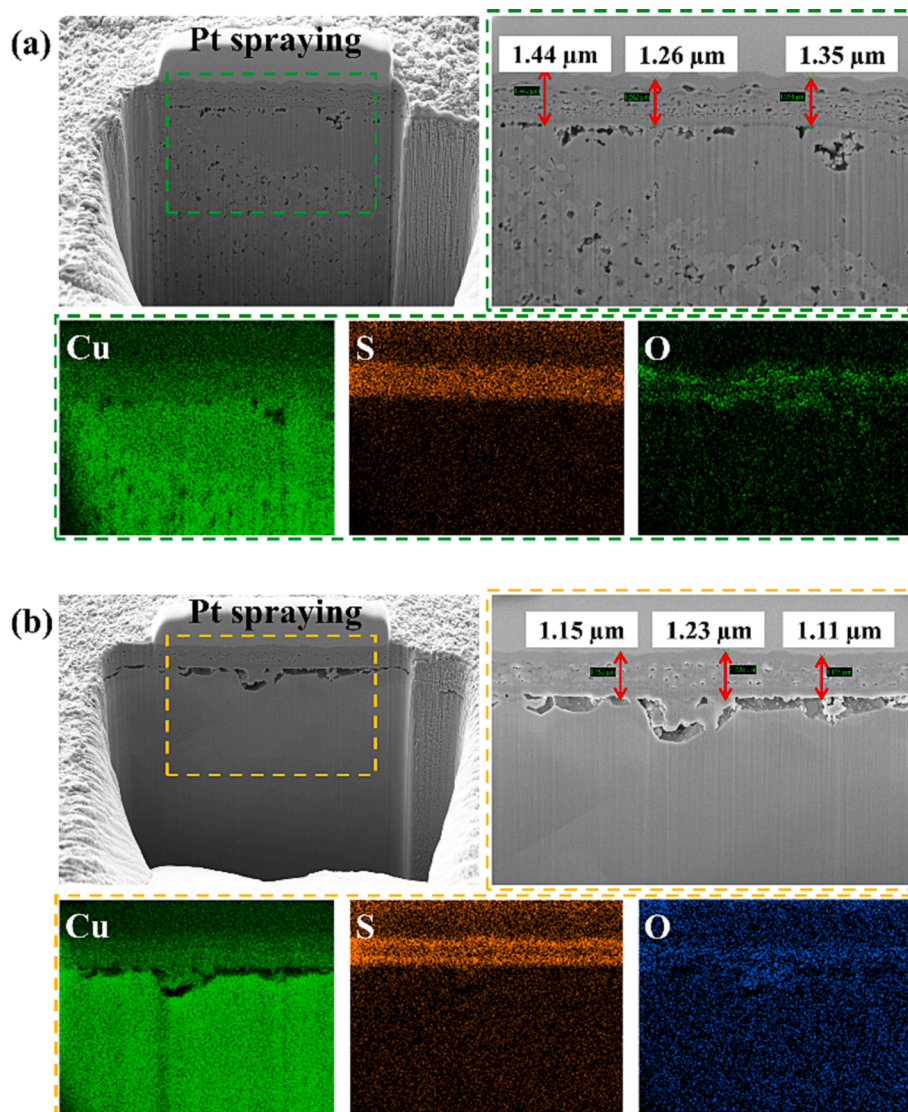

Fig. 5. FIB-generated cross-sections and SEM/EDS test results: (a) Sintered nanoCu sample and (b) bulk Cu sample.
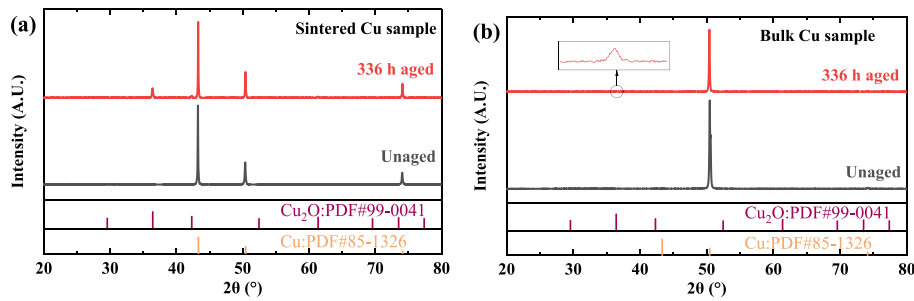
Fig. 6. XRD patterns of samples before and after aging: (a) Sintered nanoCu samples and (b) bulk Cu samples.
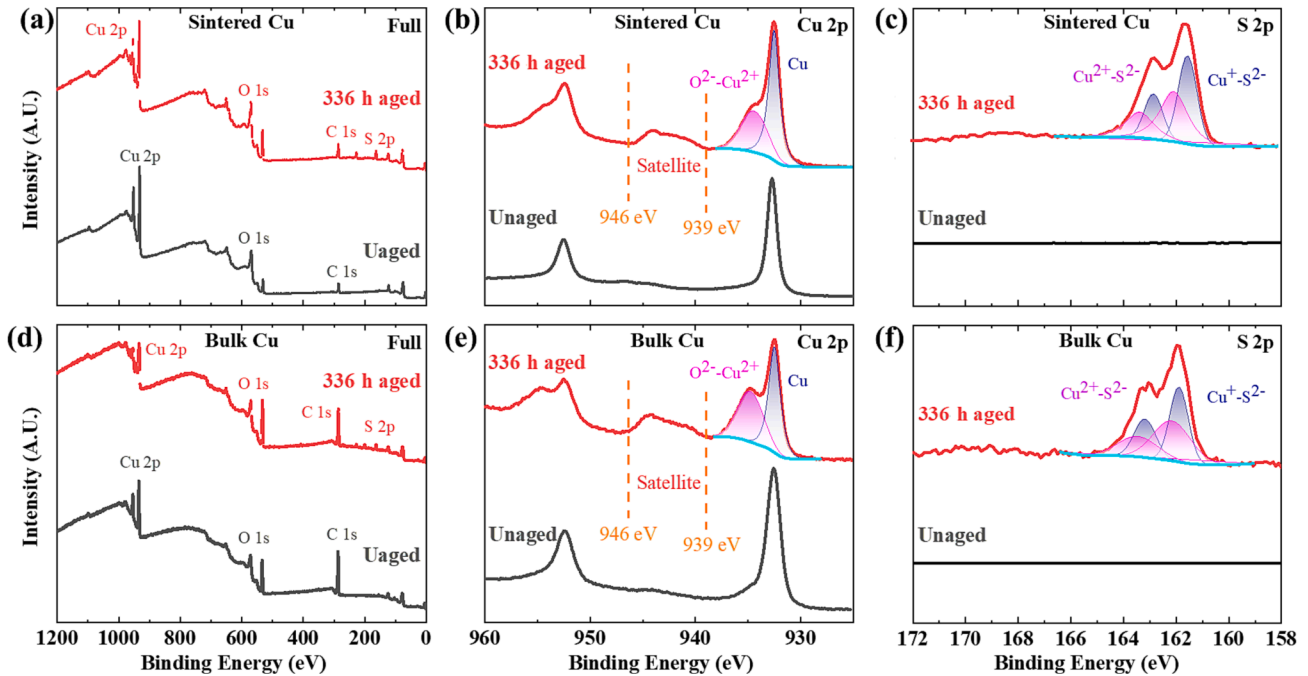

Fig. 7. (a) Full, (b) Cu 2p, and (c) S 2p XPS spectra of sintered nanoCu sample. (d) Full, (e) Cu 2p, and (f) S 2p XPS spectra of bulk Cu sample.

[45,46]. Furthermore, the peaks around 163.3 eV for Cu^{2+}-S 2p1/2 and 162.1 eV for Cu^{2+}-S 2p3/2 support the existence of CuS [47,48]. Fig. 7 (d)–(f) show the XPS spectra of the bulk Cu sample before and after aging. The XPS spectra reveal that the surface of the bulk Cu sample aged for 336 h also contained CuO, Cu_2S, and CuS. By combining the findings from XRD and XPS analyses, the corrosion products formed during H_2S aging in both the sintered and bulk Cu samples were found to be the same: Cu_2O, Cu_2S, CuO, and CuS.

The potential reactions of the sintered and bulk Cu samples during H_2S aging can be inferred from the results of testing and analysis. In an air environment containing 1 ppm H_2S gas, Cu could undergo direct chemical reactions with both O_2 and H_2S, resulting in the formation of Cu_2O [49] and Cu_2S [41], respectively. The reactions involved are as follows:

$$4Cu + O_2 \rightarrow 2Cu_2O, \tag{1}$$

$$2Cu + H_2S \rightarrow Cu_2S + H_2. \tag{2}$$

The formed Cu_2O may continue to react with either O_2 or H_2S, resulting in the formation of CuO [49] and CuS [41,50], respectively. These reactions are as follows:

$$2Cu_2O + O_2 \rightarrow 4CuO, \tag{3}$$

$$Cu_2O + H_2S \rightarrow Cu_2S + H_2O. \tag{4}$$

The produced CuO may react with H_2S, converting into CuS [51]. This reaction is as follows:

$$CuO + H_2S \rightarrow CuS + H_2O. \tag{5}$$

Under the condition of 85 % relative humidity, numerous microdroplets composed of several tens of water molecules were distributed on the surfaces of the sintered and bulk Cu samples [52]. These microdroplets provided the necessary conditions for the electrochemical reactions.

Trace amounts of O_2 from the air and Cu on the sample surface would dissolve into the microdroplets, forming OH^- and Cu^+ ions. The reactions involved are as follows:

$$Cathode\ electrode : O_2 + 2H_2O + 4e^- \rightarrow 4OH^-, \tag{6}$$

$$Anode\ electrode : Cu \rightarrow Cu^+ + e^-. \tag{7}$$
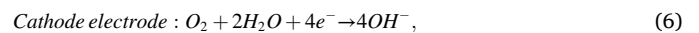
Cu^+ reacted with OH^- in the solution to generate Cu_2O [41], as follows:

$$2Cu^+ + 2OH^- \rightarrow Cu_2O + H_2O \tag{8}$$

A trace amount of Cu^+ reacted with HS^- to form Cu_2S [28], as follows:

$$H_2S + OH^- \rightarrow HS^- + H_2O, \tag{9}$$

$$2Cu^+ + HS^- \rightarrow Cu_2S + H^+. \tag{10}$$

The formation of CuS may involve a two-step dissociation of H_2S to generate S^{2-}, followed by a subsequent reaction with Cu^+ [53], as follows:

$$H_2S \rightarrow HS^- + H^+, \tag{11}$$

$$2HS^- + 2e^- \rightarrow 2S^{2-} + H_2, \tag{12}$$

$$Cu^+ + S^{2-} \rightarrow CuS + e^-. \tag{13}$$

In the H_2S^-containing environment, corrosion products such as Cu_2S, CuS, Cu_2O, and CuO were frequently observed, with Cu_2S and Cu_2O being the dominant species [27,28,41,53,54].

4. Influence of H₂S-induced corrosion on properties

To evaluate the influence of H_2S aging on intrinsic properties, this section begins by comparing the electrical resistivity, thermal conductivity, coefficient of thermal expansion, and elastic modulus of both sintered and bulk samples before and after the aging process. To assess the impact of H_2S aging on interfacial performance, the subsequent portion of this section examines the shear strength and fracture mode of the sintered nanoCu joint sample before and after aging.

4.1. Electrical resistivity

The sintered nanoCu, as a die attachment material, needs to possess a sufficiently high current-carrying capability. Consequently, the changes in the resistivity of both sintered and bulk Cu samples following exposure to corrosion were assessed. The resistivity was determined using the four-probe testing method (Fig. 8). The formula for calculating electrical resistivity (ρ) is presented below:

$$\rho = 4.532 \frac{V}{I} \times h \times K, \tag{14}$$

where V represents the voltage (μV) between the outer two probes (probes 2 and 3), I represents the current (A) between the inner two probes (probes 1 and 4), h represents the thickness (cm) of the test sample, and K is an adjustment factor associated with the probe spacing and the diameter of the inscribed circle within the sample. The K value for the present sample is 3.97.

Fig. 9 shows the evolution of the electrical resistivity of sintered and bulk Cu samples with increasing H_2S aging time. The electrical resistivity of the unaged sintered and bulk Cu samples was 1.87 μΩ·cm and 1.65 μΩ·cm, respectively. Due to the presence of voids, sintered nanoCu samples demonstrated a higher electrical resistivity value, 13.39 %

Fig. 8. Principle of linear four-probe testing.

higher than that of bulk Cu samples. As shown in Fig. 9(a), H_2S aging significantly elevated the sintered nanoCu sample's electrical resistivity. Over the course of H_2S aging spanning from 0 to 168 h, the electrical resistivity exhibited a rapid increase from 1.87 μΩ·cm to 708.08 μΩ·cm. Subsequently, during the interval of 168–264 h, the electrical resistivity experienced a substantial surge, reaching 6468.63 μΩ·cm. Due to the excessive electrical resistivity exceeding the measurement range of the equipment, the apparatus could not be used to conduct tests on samples subjected to aging for more than 264 h. As depicted in Fig. 9(b), the influence of H_2S aging on the electrical resistivity of the bulk Cu sample was considerably lower than that on the electrical resistivity of the sintered nanoCu sample. During the initial 0–120-h period, the electrical resistivity remained quite stable. Within the time span of 120–264 h, the electrical resistivity rapidly increased to 1219.55 μΩ·cm. Finally, from 264 to 366 h, the electrical resistivity experienced a pronounced increase, reaching 4516.33 μΩ·cm.

4.2. Thermal properties

Effective heat transfer is a crucial requirement for sintered nanoCu. The thermal conductivity (λ) values of both sintered and bulk Cu samples are shown in Table 1, indicating a statistically significant difference between the before and after aging groups. The thermal conductivity values of the unaged sintered and bulk Cu samples were 256.46 W/(m·K) and 399.60 W/(m·K), respectively. The sintered nanoCu sample exhibited a thermal conductivity equivalent to 64.18 % of that observed in the bulk Cu sample. After 336 h of H_2S aging, the thermal conductivity values of the sintered and bulk Cu samples were determined to be 185.66 W/(m·K) and 309.06 W/(m·K), respectively. The resultant reduction rates in thermal conductivity for the sintered and bulk Cu samples were computed as 27.61 % and 22.66 %, respectively.

The coefficient of thermal expansion (*CTE*) significantly impacts the reliability of joints in scenarios involving rapid temperature changes. The *CTE* values of sintered and bulk Cu samples were measured both before and after H_2S aging, and the corresponding results are graphically depicted in Fig. 10. The change in the thermal strain of the samples with changing temperatures is depicted in Fig. 10(a) and (b). Based on the strain results, the *CTE* value can be calculated as follows:

$$CTE = \frac{\Delta L \times K_{CTE}}{L \times \Delta T}, \tag{15}$$

where L and ΔL are the sample's initial length and the change in length within the temperature difference (ΔT), respectively. K_{CTE} is the calibration coefficient, and the K_{CTE} value is 1 in this study. The calculated *CTE* results are shown in Fig. 10(c) and (d). The *CTE* value for unaged sintered and bulk Cu samples remained constant at 21.8 ppm/°C and 18.5 ppm/°C, respectively, over the temperature range of 30–200 °C. The *CTE* of the sintered nanoCu sample was 21.11 % higher than that of the bulk Cu sample. This may be attributed to the swift expansion of the gas volume within sealed voids in sintered nanoCu upon heating. After 336 h of H_2S aging, the *CTE* value of the sintered nanoCu sample became lower than that of the unaged sample, except within the temperature range of 150–175 °C, where the *CTE* showed pronounced fluctuations. Further, the *CTE* value of the bulk Cu sample consistently remained lower than that of the unaged sample.

4.3. Mechanical properties

H_2S aging induced changes in the surface morphology and elemental distribution of both the sintered and bulk Cu samples. Nanoindentation test was employed to assess the impact of corrosion on the surface elastic modulus (*E*). Each sample underwent 40 nanoindentation tests, with the indentation sites arranged in a 5 × 10 array. The indentation positions were separated by 50 μm in both the x and y directions, resulting in an indented area of 200 × 450 μm. Nanoindentation testing was conducted
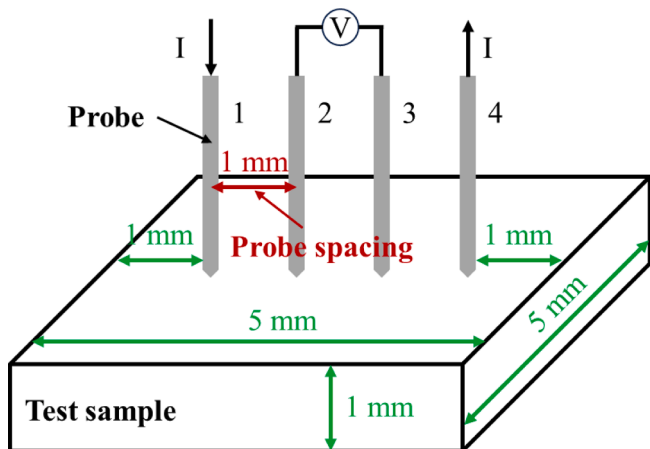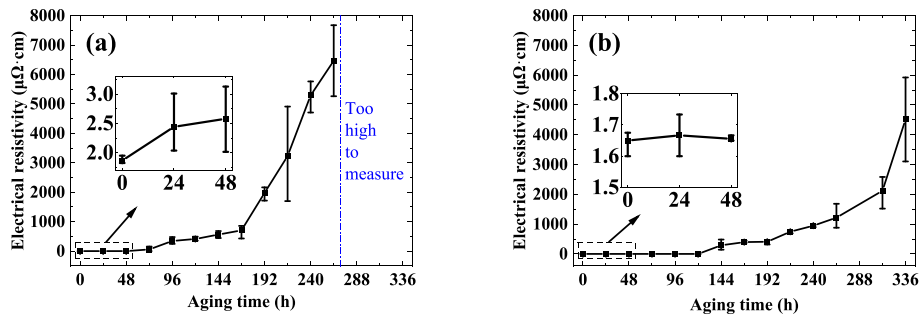
Fig. 9. Evolution of electrical resistivity under H_2S aging: (a) Sintered nanoCu sample and (b) bulk Cu sample.

Table 1
Influence of H_2S-aging on the thermal conductivity of sintered and bulk Cu samples.

Samples	Mean λ [W/(m·K)]	Standard deviation of λ [W/(m·K)]
Unaged sintered nanoCu	256.46	21.05
336 h of H_2S aged Sintered nanoCu	185.66	33.81
P value	< 0.001	
Unaged bulk Cu	399.60	13.52
336 h of H_2S aged bulk Cu	309.06	46.07
P value	< 0.001	

in accordance with the standard ISO 14577. A test load of 50 mN was applied at a loading rate of 5 mN/s.

Table 2 presents the E values obtained through nanoindentation tests for various samples, showing a statistically significant difference between the before and after aging groups. Under the initial condition, the mean E values for the sintered and bulk Cu samples were 139.24 MPa and 160.02 MPa, respectively. Following sintering, the E value for the sintered nanoCu samples became 12.99 % lower than that of the bulk Cu samples. After 336 h of H_2S aging, the mean E values for the sintered and bulk Cu samples decreased to 53.95 MPa and 68.13 MPa, respectively, corresponding to a reduction of 61.25 % and 57.42 %, respectively. The indentation regions are illustrated in Fig. 11(a), and Fig. 11(b) shows the distribution of E within the testing area. The E value distribution across various regions on the surfaces of the four samples was evidently highly consistent, and the small standard deviation among the four samples further supported this observation. In general, the extent of decrease in the elastic modulus of the sintered nanoCu sample due to H_2S aging was slightly greater than that of the bulk Cu sample.

4.4. Fracture behavior of joints

The die attachment process using low-temperature joining technique (LTJT) with Cu nanoparticles can be carried out below 400 °C, leading to low-porosity sintered nanoCu with melting points similar to those of

Table 2
Influence of H_2S aging on elasticity modulus (E) of sintered and bulk Cu samples.

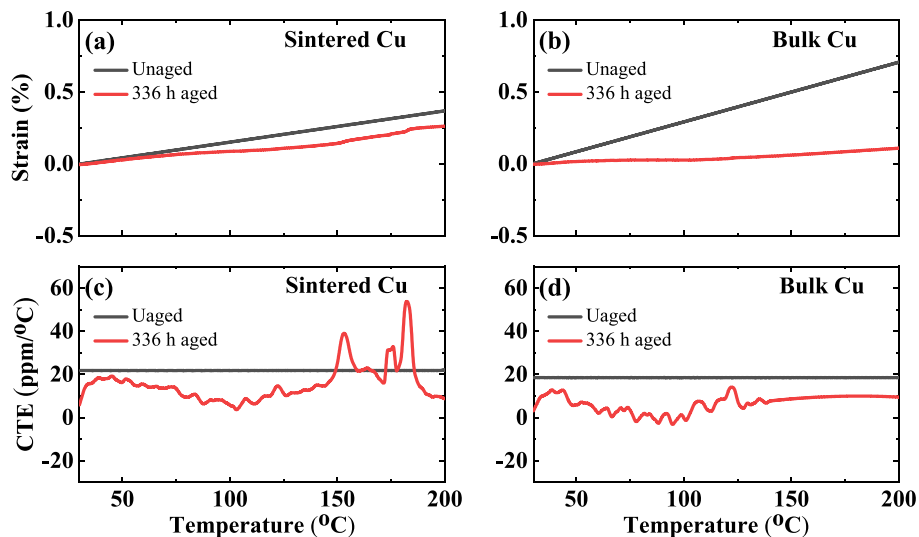| Samples	Mean E (MPa)	Standard deviation of E (MPa)
Unaged sintered nanoCu	139.24	8.63
336 h of H_2S aged sintered nanoCu	53.95	10.86
P value	< 0.001	
Unaged bulk Cu	160.02	7.80
336 h of H_2S aged bulk Cu	68.13	8.99
P value	< 0.001	

Fig. 10. Thermal strain from 30 °C to 200 °C for (a) sintered and (b) bulk Cu samples. Coefficient of thermal expansion from 30 °C to 200 °C for (c) sintered and (d) bulk Cu samples.
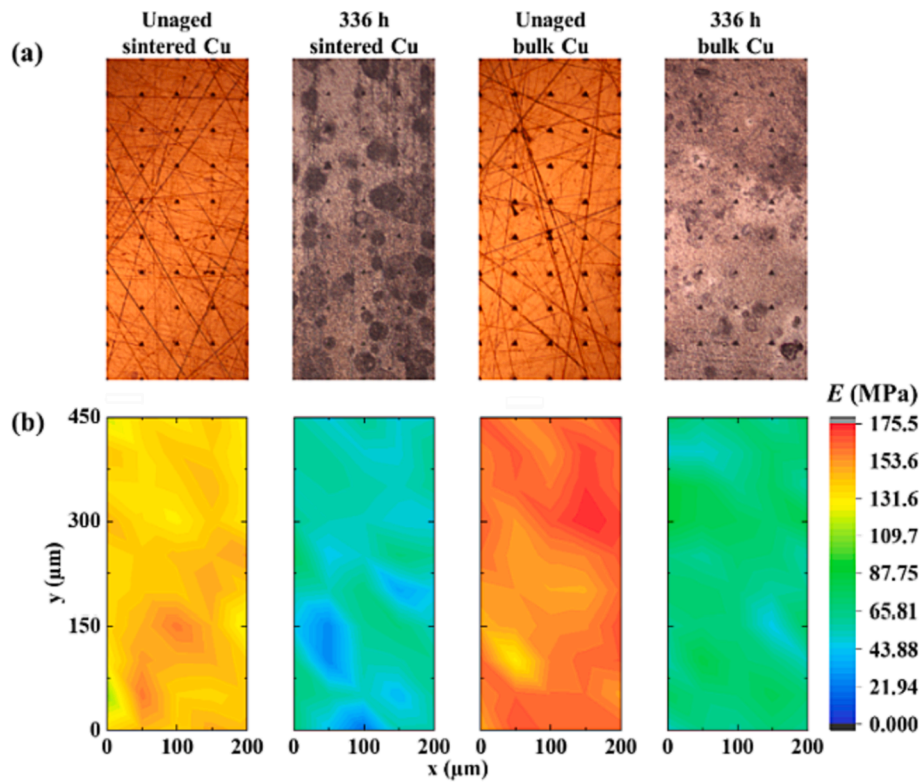
Fig. 11. (a) Nanoindentation test regions of different samples. (b) Elasticity modulus (E) distributions in each test region.
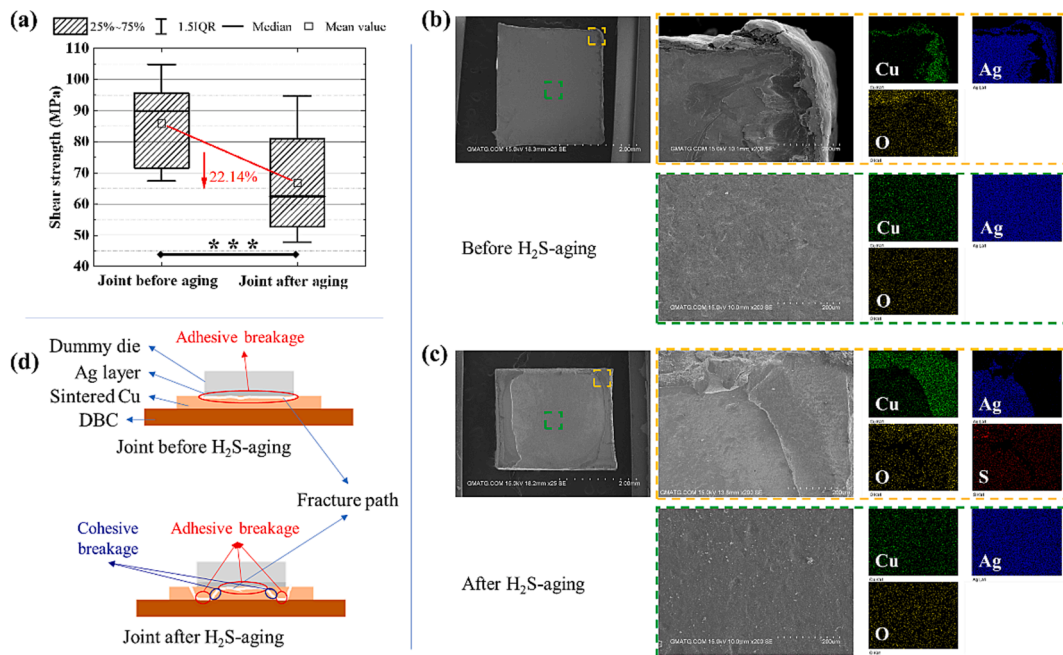

Fig. 12. (a) Shear strength with statistically significant difference between groups (* * *p < 0.001), (b) and (c) fracture surface morphologies on the dummy die and (d) schematics illustrating the fracture routes of sintered nanoCu joints before and after H_2S aging.

bulk metals. For the evaluation of attachment properties, the shear strength of sintered nanoCu joints was determined through shear testing. A set of six joint samples both before and after H_2S aging were subjected to testing, and the results of these assessments are presented in Fig. 12(a), with statistically significant difference between groups (* * *p < 0.001). After H_2S aging, the sintered nanoCu joints exhibited a shift in the mean shear strength from 85.88 MPa to 66.68 MPa, i.e., a

reduction rate of 22.14 %. In addition, the shear strength variation increased following the aging process. This observation indicates that H_2S aging significantly deteriorates the interconnectivity performance of sintered nanoCu. Notably, even after H_2S aging, the shear strength of the joints investigated in this study continues to significantly exceed the industrially acceptable threshold of 30 MPa [15,55].

The surface morphologies after shear fracture were examined using

SEM/EDS to analyze the fracture modes. The fracture surface morphologies on the dummy die are shown in Fig. 12(b). In the case of dummy die joints before H$_2$S aging, fractures primarily manifested at the interface between the sintered copper and the silver layer coated on the surface of the dummy die. The presence of a small amount of Cu element was observed in both the edge and central regions. This confirms the establishment of a sturdy mechanical connection between the sintered nanoCu and the Ag layer. However, no substantial amount of sintered nanoCu was present in the dummy die. This means that the adhesive strength between the sintered body and the Ag layer was inferior to the cohesive strength of the sintered body and the adhesive strength between the sintered body and the Cu layer in DBC.

The results for dummy die joints after 336 h of H$_2$S aging are presented in Fig. 12(c). The sintered nanoCu layer was still observed at the edge of the dummy die. Trace amounts of S were distributed across the edge of the dummy die and the fracture surface of the sintered nanoCu. However, no elemental S was found in the central regions of the dummy die. This observation indicates the penetration of S into the edge of the sintered nanoCu layer. When compared to the adhesive strength between the sintered nanoCu and the Ag layer, the penetration resulted in a greater reduction in the cohesive strength of the sintered nanoCu and the adhesive strength between the sintered nanoCu and the Ag layer.

A schematic diagram illustrating the fracture paths of the sintered nanoCu joints is presented in Fig. 12(d). Typically, in unaged joint structures, the fracture path emerged at the interface between the sintered nanoCu and the Ag layer, resulting from adhesive breakage. However, in the H$_2$S-aged joint structures, additional fractures were observed within the sintered nanoCu and at the interface between the edge of the sintered nanoCu and DBC, and these were attributed to a combination of adhesive and cohesive breakages.

To study the corrosion within the joints, cross-sectional samples of SiC die joints after 336 h of H$_2$S aging were prepared and observed using SEM/EDS analysis, and the results are presented in Fig. 13. Fig. 13(a) illustrates the SiC die, the sintered nanoCu layer, and the DBC structure, with the sintered nanoCu layer having an approximate thickness of 30 μm. Fig. 13(b) reveals pronounced elemental S penetration in the SiC die uncovered area and slight S corrosion in the SiC die covered area. However, the light S corrosion substantially reduced the shear strength of the die interconnect structure.

5. Penetration mechanisms of H$_2$S and O$_2$ into sintered and bulk Cu samples

The penetration mechanism of H$_2$S and O$_2$ into both sintered and bulk Cu configurations is analyzed through Reactive Force Field (ReaxFF) MD simulations.

5.1. Computational methods

The experimental tracking of atomic-level shifts during the corrosion process is difficult. Therefore, MD simulations were executed in the

Large-scale Atomic/Molecular Massively Parallel Simulator (LAMMP) [56]. These simulations first mimicked the pressure-assisted sintering of Cu nanoparticles, followed by the H$_2$S-induced sulfidation of sintered and bulk Cu samples. The resulting computations were visually represented in three dimensions using the Open Visualization Tool (OVITO) [57], providing a comprehensive depiction of the findings.

To simulate pressure-assisted sintering, the classical embedded-atom method (EAM) potential [58] was employed to describe the interactions among Cu atoms. Its selection was based on advantages: fewer parameters, faster convergence, lower errors, higher precision, and enhanced capability in simulating interatomic interactions across multiple scales. The total energy E_{tot} can be represented as follows [59]:

$$E_{tot} = \sum_i F_i(\theta_{h,i}) + 0.5\sum_{i=1}\sum_{j(j\neq i)} q_{ij}(R_{ij}), \tag{16}$$

where $\theta_{h,i}$, $F_i(\theta)$, and $q_{ij}(R_{ij})$ are the host electron density of the ith atom, the energy to embed the ith atom into the background electron density ρ, and the core–core pair repulsion between i^{th} and j^{th} atoms with a distance of R_{ij}, respectively.

Further, ReaxFF with Cu/H/S/O elements [22,60] was employed to model the reactive chemistry, including bond formation and breaking. E_{tot} can be represented as follows:

$$E_{tot} = E_{bond} + E_{over} + E_{under} + E_{H-bond} + E_{lp} + E_{val} + E_{tors} + E_{vdWaals} + E_{coulomb}, \tag{17}$$

where E_{bond}, E_{over}, E_{under}, and E_{H-bond} represent the bond energy, over-coordination energy, under-coordination energy, and hydrogen bond energy, respectively, all of which are bond-order-dependent interactions. In addition, E_{tors}, E_{val}, and E_{lp} correspond to the torsion angle energy, valence angle energy, and lone pair energy, respectively, all of which are covalent interactions. Further, $E_{vdWaals}$ and $E_{Coulomb}$ denote van der Waals energy and Coulomb energy, respectively, both of which are non-bonded interactions.

5.2. Simulation details

In this study, all simulated systems had periodic boundaries and underwent energy minimization using the conjugate gradient algorithm (CGA). The dimensions of the simulation cell were 36 Å × 36 Å × 110 Å. To simulate pressure-assisted sintering, a system of multiple Cu nanoclusters, each with a diameter of 1.278 nm, arranged in face-centered-cubic stacking, was constructed with a total of 2784 Cu atoms. The sintering process was simulated using the NPT (isothermal–isobaric) ensemble. The temperature and pressure of the simulation cell were maintained at 523 K and 20 MPa, respectively. The sintering process was carried out for a duration of 200 ps.

To simulate the corrosion process of sintered and bulk Cu samples in H$_2$S-containing air environment, a mixture of gases including H$_2$S, O$_2$, and H$_2$O was introduced into the simulation cells of both the sintered and bulk Cu samples, with an approximate distance of 10 Å from the Cu
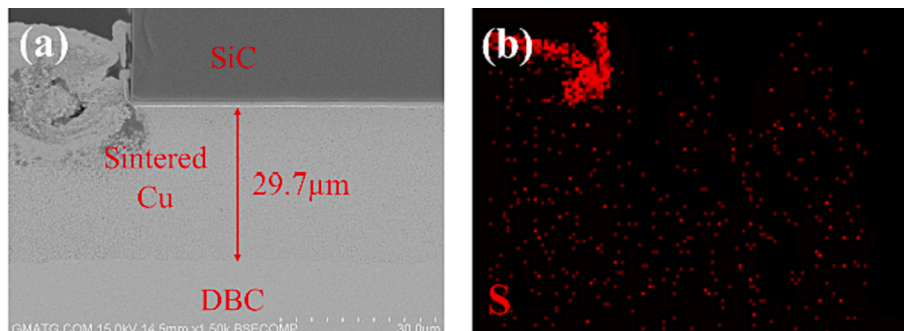

Fig. 13. Cross-section morphologies of SiC die joints after H$_2$S aging: (a) SEM and (b) EDS mapping for S element.
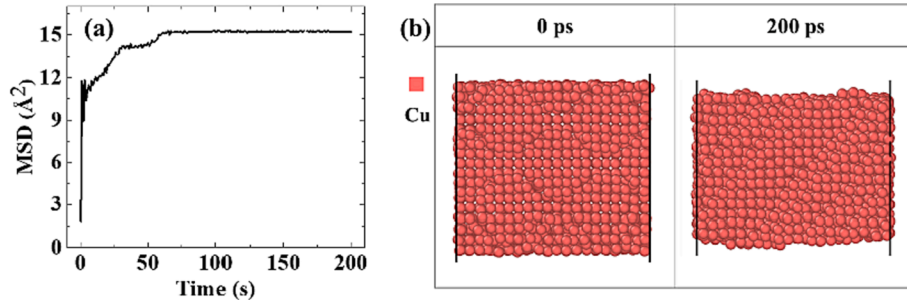
Fig. 14. Pressure-assisted sintering process: (a) evolution and (b) atomic configuration evolution.

surface. The number of molecules for H_2S, O_2, and H_2O is all 50. Notably, the bulk Cu configuration includes 4000 atoms arranged in a crystalline structure. The simulations were conducted under the NVT (canonical) ensemble. The temperature of the simulation cell was regulated to 318 K using the Nose–Hoover thermostat. To ensure thorough sulfidation, the corrosion process was sustained for a duration of 200 ps.

5.3. Analysis of sintering process

The displacement of Cu atoms during the sintering process was characterized using mean-square displacement (MSD), given by

$$MSD = \frac{1}{N} \sum_{i=1}^{N} \left[r_i(t) - r_i(0) \right]^2, \tag{18}$$

where $r_i(0)$ and $r_i(t)$ denote the position of the ith Cu atom at the initial time and time t, and N is the total number of Cu atoms. The results of the MSD analysis are depicted in Fig. 14(a). Between 0 and 60 ps, the MSD values progressively increased with time, indicating the rapid diffusion of atoms within distinct Cu nanoparticles. From 60 ps to 200 ps, the MSD values remained stable, signifying the completion of the sintering process. During the process of pressure-assisted sintering, Cu atoms in nanoparticles came into contact and formed neck regions, leading to the development of a densified structure. The evolution of the atomic configuration is presented in Fig. 14(b). The results demonstrate a reduction in the atomic volume for the Cu configuration as the sintering process advances. Computational analysis shows that the sintering

process induces a decrease in the volume of sintered nanoCu configuration by 19.22 %. The sintered nanoCu configuration exhibits a density of 7.77 g/cm^3, corresponding to 87.3 % of the density observed in bulk Cu.

5.4. Analysis of sulfidation process

Fig. 15(a) and (b) illustrate the atomistic progressions of H_2S and O_2 penetration into the sintered and bulk Cu configurations, showing that the majority of gas molecules diffused into the sintered and bulk Cu samples. Subsequently, the penetration depth of H_2S and O_2 into the sintered and bulk Cu configurations was quantified, and the results are presented in Fig. 15(c) and (d). In both the sintered and bulk Cu configurations, the penetration depth of H_2S and O_2 exceeded 4 Å, indicating chemical reactions between H_2S, O_2 and Cu. During the penetration process, Cu atoms on the surfaces of the sintered and bulk Cu configurations also exhibit significant upward movement, and the distances are shown in Fig. 15(e) and (f). Several layers of Cu atoms near the surface undergo substantial displacement, resulting in lattice distortions. The H_2S-induced corrosion mechanisms of sintered nanoCu and bulk Cu can be summarized as follows: H_2S and O_2 penetrated into the Cu configurations, accompanied by the upward migration of molecules from the upper layers of the Cu configurations. Their combined action resulted in the formation of a corrosion film.

For both sintered and bulk Cu configurations, H_2S and O_2 rapidly reached their maximum penetration depths within 25 ps, after which the penetration depth remained stable with slight fluctuations. The sintered nanoCu configurations exhibited H_2S and O_2 penetration depths greater
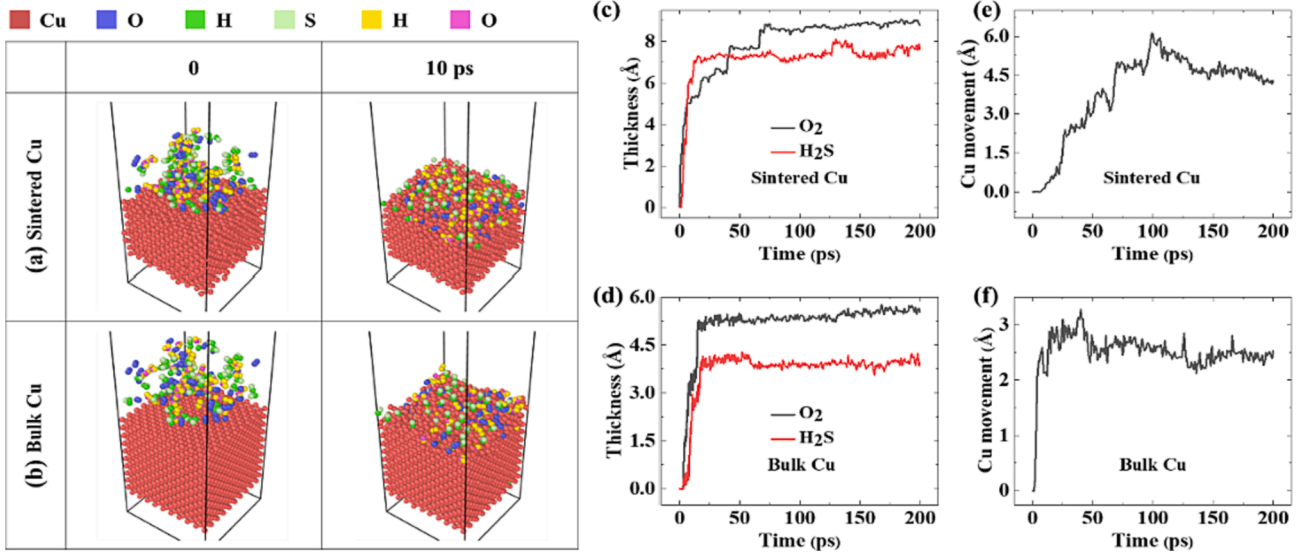

Fig. 15. (a)–(b) Atomistic configuration evolutions, (c)–(d) H_2S and O_2 penetration depths, and (e)–(f) distances traversed by Cu atoms of sintered and bulk Cu configurations.

than those of bulk Cu configurations, and the upward distances traversed by Cu atoms were also greater in the case of sintered samples. The presence of voids within the sintered nanoCu configuration allows H_2S and O_2 to either more easily diffuse through these voids or more easily traverse among enclosed voids, resulting in deeper penetration. Due to the pristine crystalline structure of bulk Cu configuration, the penetration of H_2S into the bulk Cu configuration can be relatively challenging. Further, the weaker bond strength between Cu nanoparticles also resulted in a greater propensity for Cu atoms to move upward in the sintered nanoCu configurations. This is also the reason why the sintered nanoCu sample exhibits more severe corrosion and performance degradation. The die attachment process using Cu nanoparticles results in the formation of voids [14]. The enhancement of the sintering process can reduce these voids and improve the corrosion resistance of sintered nanoCu. Another promising approach is the addition of other nanoparticles into the sintered nanoCu paste, such as Pd [61] and Si [55], similar to the technique validated in the case of sintered Ag.

6. Conclusions

This study involved aging sintered nanoCu using 1 ppm H_2S for 336 h, comparing it with bulk Cu. The corrosion phenomena, products, and mechanisms were analyzed. Additionally, the changes in electrical, thermal, and mechanical properties post-H_2S aging for both sintered and bulk Cu samples were investigated, focusing on the impact on interconnect performance. ReaxFF MD simulations probed H_2S and O_2 penetration in sintered and bulk Cu configurations, unveiling H_2S-induced aging mechanisms. The key findings are: (1) Initially, both sintered nanoCu and bulk Cu preferred reacting with O_2 before H_2S. As aging progressed, corrosion products fractured and detached, allowing continued gas reactions. Notably, sintered nanoCu exhibited more severe corrosion. (2) H_2S aging led to increased electrical resistivity, reduced thermal conductivity, thermal expansion coefficient, and elastic modulus in both sintered and bulk Cu, with sintered nanoCu showing greater degradation. It also caused decreased shear stress at the edge of sintered nanoCu joints, altering the failure mode. (3) H_2S and O_2 penetration induced surface Cu movement, contributing to corrosion layer formation. Deeper penetration in sintered nanoCu explained its more significant degradation. O_2 penetrated deeper than H_2S, influencing Cu's preference for reaction. This study offers insights into sintered nanoCu and bulk Cu corrosion in H_2S-containing environments, beneficial for developing corrosion-resistant electronic devices in challenging settings. Further studies should focus on enhancing sintered nanoCu's corrosion resistance through improved processes or nanoparticle additions.

CRediT authorship contribution statement

Wei Chen: Writing – original draft, Visualization, Methodology, Investigation, Formal analysis, Data curation. **Xu Liu:** Visualization, Investigation, Data curation. **Dong Hu:** Writing – review & editing. **Xi Zhu:** Writing – review & editing. **Xuejun Fan:** Supervision. **Guoqi Zhang:** Supervision. **Jiajie Fan:** Validation, Supervision, Software, Resources, Project administration, Funding acquisition, Conceptualization.

Declaration of competing interest

The authors declare that they have no known competing financial interests or personal relationships that could have appeared to influence the work reported in this paper.

Data availability

Data will be made available on request.

References

[1] X. Zhong, X. Wu, W. Zhou, K. Sheng, An all-sic high-frequency boost DC–DC converter operating at 320 °C junction temperature, IEEE Trans. Power Electron. 29 (10) (2014) 5091–5096.

[2] B.J. Baliga, Silicon Carbide Power Devices, in: M. Rudan, R. Brunetti, S. Reggiani (Eds.), Springer Handbook of Semiconductor Devices, Springer International Publishing, Cham, 2023, pp. 491–523.

[3] A. Kar, K. Kundu, H. Chattopadhyay, R. Banerjee, White light emission of wide-bandgap silicon carbide: a review, J. Am. Ceram. Soc. 105 (5) (2022) 3100–3115.

[4] H. Zhou, A. Chang, J. Fan, J. Cao, B. An, J. Xia, J. Yao, X. Cui, Y. Zhang, Copper wire bonding: a review, Micromachines 14 (8) (2023) 1612.

[5] R. Chowdhury, K. Young, T.J. Poche, S. Jang, Effect of dual sintering with laser irradiation and thermal treatment on printed copper nanoparticle patterns, Nanotechnology 34 (42) (2023) 425704.

[6] G.Q. Zhang, M. Graef, F.V. Roosmalen, The rationale and paradigm of "more than Moore", in: 56th Electronic Components and Technology Conference 2006, 2006, pp. 151–157.

[7] L. Wang, T. Zhang, F. Yang, D. Ma, C. Zhao, Y. Pei, Y. Gan, Cu Clip-bonding method with optimized source inductance for current Balancing in multichip SiC MOSFET power module, IEEE Trans. Power Electron. 37 (7) (2022) 7952–7964.

[8] Z. Huang, Y. Li, L. Chen, Y. Tan, C. Chen, Y. Kang, F. Luo, A novel low inductive 3D SiC power module based on hybrid packaging and integration method, IEEE Energy Conversion Congress Exposition (ECCE) 2017 (2017) 3995–4002.

[9] W. Mu, L. Wang, B. Wang, T. Zhang, F. Yang, Y. Gan, H. Zhang, Direct integration of optimized phase-change heat spreaders Into SiC power module for thermal performance improvements under high heat flux, IEEE Trans. Power Electron. 37 (5) (2022) 5398–5412.

[10] K.-C. Shie, P.-N. Hsu, Y.-J. Li, D.-P. Tran, C. Chen, Failure Mechanisms of Cu–Cu Bumps under Thermal Cycling, Materials 14 (19) (2021) 5522.

[11] W. Chen, J. Jiang, A.H. Meda, M.S. Ibrahim, G. Zhang, J. Fan, A thin and low-inductance 1200 V SiC MOSFET fan-out panel-level packaging with thermal cycling reliability evaluation, IEEE Trans. Electron Devices 70 (5) (2023) 2268–2275.

[12] H.R. Kotadia, P.D. Howes, S.H. Mannan, A review: On the development of low melting temperature Pb-free solders, Microelectron. Reliab. 54 (6) (2014) 1253–1273.

[13] T. Laurila, V. Vuorinen, M. Paulasto-Kröckel, Impurity and alloying effects on interfacial reaction layers in Pb-free soldering, Mater. Sci. Eng. R. Rep. 68 (1) (2010) 1–38.

[14] X. Liu, S. Li, J. Fan, J. Jiang, Y. Liu, H. Ye, G. Zhang, Microstructural evolution, fracture behavior and bonding mechanisms study of copper sintering on bare DBC substrate for SiC power electronics packaging, J. Mater. Res. Technol. 19 (2022) 1407–1421.

[15] T.F. Chen, K.S. Siow, Comparing the mechanical and thermal-electrical properties of sintered copper (Cu) and sintered silver (Ag) joints, J. Alloys Compounds 866 (2021) 158783.

[16] J. Dai, Y. Wang, T. Grant, W. Wang, M. Mat, M. Morshed, High temperature reliability of pressureless sintered Cu joints for power SiC die attachment, Microelectron. Reliab. 150 (2023) 115219.

[17] J. Chen, Y. Gong, Z.-G. Yang, Failure analysis on the pin fin heat sink for the power module of new energy vehicles, Eng. Fail. Anal. 143 (2023) 106870.

[18] Y. Wang, E. Deng, L. Wu, Y. Yan, Y. Zhao, Y. Huang, Influence of humidity on the power cycling lifetime of SiC MOSFETs, IEEE Trans. Compon. Packag. Manuf. Technol. 12 (11) (2022) 1781–1790.

[19] P. Singh, L. Palmer, M. Smith, D.S. Citrin, A. Locquet, D. Hampannavar, H. Fu, M. M. Khaw, K.L. Tan, C. Xu, J. Kaufman, M. Pudas, H. Schweigart, S. Strixner, M. R. Meier, C. Wang, H. Akbari, Comparing various test environments for conformal coating evaluation, Int. Conf. Electron. Packaging (ICEP) 2022 (2022) 89–90.

[20] S.K. Bhogaraju, H.R. Kotadia, F. Conti, A. Mauser, T. Rubenbauer, R. Bruetting, M. Schneider-Ramelow, G. Elger, Die-Attach Bonding with Etched Micro Brass Metal Pigment Flakes for High-Power Electronics Packaging, ACS Applied Electronic Materials 3 (10) (2021) 4587–4603.

[21] L. Feng, H. Shen, Y. Zhu, H. Gao, X. Yao, Insight into generation and evolution of sea-salt aerosols from field measurements in diversified marine and coastal atmospheres, Sci. Rep. 7 (1) (2017) 41260.

[22] X. Wang, Z. Yang, B. Wang, W. Chen, G. Zhang, J. Zhang, J. Fan, P. Liu, Effect of epoxy resin addition on properties and corrosion behavior of sintered joints in power modules serviced offshore, J. Mater. Res. Technol. 25 (2023) 6593–6612.

[23] D. Minzari, M.S. Jellesen, P. Møller, R. Ambat, Morphological study of silver corrosion in highly aggressive sulfur environments, Eng. Fail. Anal. 18 (8) (2011) 2126–2136.

[24] W. Zhang, Y. Lee, Y. Zhang, A Failure Analysis of a SOP IC Creep Corrosion on power module, in: 2019 IEEE 26th International Symposium on Physical and Failure Analysis of Integrated Circuits (IPFA), 2019, pp. 1–4.

[25] M. Wang, Q. Du, Y. Li, J. Xu, J. Gao, H. Wang, Effect of steam on the transformation of sulfur during demineralized coal pyrolysis, J. Anal. Appl. Pyrol. 140 (2019) 161–169.

[26] I. Manconi, P.N.L. Lens, Removal of H2S and volatile organic sulfur compounds by silicone membrane extraction, J. Chem. Technol. Biotechnol. 84 (1) (2009) 69–77.

[27] J. Becker, J. Pellé, S. Rioual, B. Lescop, N. Le Bozec, D. Thierry, Atmospheric corrosion of silver, copper and nickel exposed to hydrogen sulphide: a multi-analytical investigation approach, Corros. Sci. 209 (2022) 110726.

[28] T.T.M. Tran, C. Fiaud, E.M.M. Sutter, Oxide and sulphide layers on copper exposed to H2S containing moist air, Corros. Sci. 47 (7) (2005) 1724–1737.

[29] C.-F. Yu, C.-M. Chan, L.-C. Chan, K.-C. Hsieh, Cu wire bond microstructure analysis and failure mechanism, Microelectron. Reliab. 51 (1) (2011) 119–124.

[30] P. Xu, Q. Fu, M. Zhao, The influence of calcium on copper corrosion and its by-product release in drinking water, RSC Adv. 13 (26) (2023) 17842–17855.

[31] C.F. Bayer, A. Diepgen, T. Filippi, C. Fuchs, S. Wuestefeld, S. Kellner, U. Waltrich, A. Schletz, Electrochemical corrosion on ceramic substrates for power electronics - causes, phenomenological description, in: and Outlook, 10th International Conference on Integrated Power Electronics Systems, 2018, pp. 1–7.

[32] T.N. Wassermann, O. Schilling, K. Müller, A.D. Rossin, J. Uhlig, A new high-voltage H2S single noxious gas reliability test for power modules, Microelectron. Reliab. 100–101 (2019) 113468.

[33] S.H. Tan, S.H. Ong, A dry migration? copper dendrite growth in adhesive tape during burn-in, in: Proceedings of the 2001 8th International Symposium on the Physical and Failure Analysis of Integrated Circuits. IPFA, 2001, 2001,, pp. 178–182.

[34] C.-J. Lee, D.-G. Kang, B.-U. Hwang, K.D. Min, J. Joo, S.-B. Jung, Fabrication of an IPL-sintered Cu circuit and its electrochemical migration behavior, J. Alloy. Compd. 863 (2021) 158726.

[35] I.B. Obot, K. Haruna, T.A. Saleh, Atomistic simulation: a unique and powerful computational tool for corrosion inhibition research, Arab. J. Sci. Eng. 44 (1) (2019) 1–32.

[36] S. Wan, Z. Dong, X. Guo, Investigation on initial atmospheric corrosion of copper and inhibition performance of 2-phenyl imidazoline based on electrical resistance sensors, Mater. Chem. Phys. 262 (2021) 124321.

[37] T. Ma, B. Tan, L. Guo, S. Kaya, Z. Kao, S. Zhang, R. Wang, N. Zeng, Y. He, Multidimensional insights into the corrosion inhibition of potassium oleate on Cu in alkaline medium: a combined Experimental and theoretical investigation, Mater. Sci. Eng. B 272 (2021) 115330.

[38] B. Tan, S. Zhang, Y. Qiang, W. Li, H. Li, L. Feng, L. Guo, C. Xu, S. Chen, G. Zhang, Experimental and theoretical studies on the inhibition properties of three diphenyl disulfide derivatives on copper corrosion in acid medium, J. Mol. Liq. 298 (2020) 111975.

[39] H. Zhou, K. Zhang, L. Zhang, J. Lu, J. Li, D. Zhang, L. Gao, A novel method to protect bronze in atmospheric environment: the click-assembly of triazole film, Anti-Corros. Methods Mater. 67 (3) (2020) 295–304.

[40] M. Reid, J. Punch, C. Ryan, L.F. Garfias, S. Belochapkine, J.P. Franey, G.E. Derkits, W.D. Reents, Microstructural development of copper sulfide on copper exposed to humid H2S, J. Electrochem. Soc. 154 (4) (2007) C209.

[41] M. Watanabe, M. Takaya, T. Handa, J. Sakai, Characterisation of corrosion products formed on copper exposed at indoor and outdoor sites with high H2S concentrations, Corros. Eng. Sci. Technol. 48 (6) (2013) 418–425.

[42] B.R. Strohmeier, D.E. Levden, R.S. Field, D.M. Hercules, Surface spectroscopic characterization of CuAl2O3 catalysts, J. Catal. 94 (2) (1985) 514–530.

[43] F.M. Capece, V.D. Castro, C. Furlani, G. Mattogno, C. Fragale, M. Gargano, M. Rossi, "Copper chromite" Catalysts: XPS structure elucidation and correlation

[44] with catalytic activity, J. Electron Spectrosc. Relat. Phenom. 27 (2) (1982) 119–128.

[44] H. Sun, O.A. Zelekew, X. Chen, Y. Guo, D.-H. Kuo, Q. Lu, J. Lin, A noble bimetal oxysulfide CuVOS catalyst for highly efficient catalytic reduction of 4-nitrophenol and organic dyes, RSC Adv. 9 (55) (2019) 31828–31839.

[45] L. Jin, L. Cai, D. Chen, W. Wang, H. Shen, F. Zhang, Efficient silicon solar cells applying cuprous sulfide as hole-selective contact, J. Mater. Sci. 54 (19) (2019) 12650–12658.

[46] Z. Yang, B. Wang, Y. Chen, W. Zhou, H. Li, R. Zhao, X. Li, T. Zhang, F. Bu, Z. Zhao, W. Li, D. Chao, D. Zhao, Activating sulfur oxidation reaction via six-electron redox mesocrystal NiS2 for sulfur-based aqueous batteries, Natl. Sci. Rev. 10 (6) (2023) nwac268.

[47] S. Tarachand, N.P. Hussain, Y.K. Lalla, A. Kuo, V.G. Lakhani, U. Sathe, G. S. Deshpande, Okram, Thermoelectric properties of Ag-doped CuS nanocomposites synthesized by a facile polyol method, PCCP 20 (8) (2018) 5926–5935.

[48] N. Karikalan, R. Karthik, S.-M. Chen, C. Karuppiah, A. Elangovan, Sonochemical synthesis of sulfur doped reduced graphene oxide supported CuS nanoparticles for the non-enzymatic glucose sensor applications, Sci. Rep. 7 (1) (2017) 2494.

[49] Y. Unutulmazsoy, C. Cancellieri, M. Chiodi, S. Siol, L. Lin, L.P.H. Jeurgens, In situ oxidation studies of Cu thin films: Growth kinetics and oxide phase evolution, J. Appl. Phys. 127 (6) (2020) 065101.

[50] J.L. Sansregret, Reaction of copper oxide with H2S, J. Electrochem. Soc. 127 (9) (1980) 2083.

[51] K. Mikami, Y. Kido, Y. Akaishi, A. Quitain, T. Kida, Synthesis of Cu2O/CuO Nanocrystals and Their Application to H2S Sensing, Sensors 19 (1) (2019) s19010211.

[52] A.L. Sumner, E.J. Menke, Y. Dubowski, J.T. Newberg, R.M. Penner, J. C. Hemminger, L.M. Wingen, T. Brauers, B.J. Finlayson-Pitts, The nature of water on surfaces of laboratory systems and implications for heterogeneous chemistry in the troposphere, PCCP 6 (3) (2004) 604–613.

[53] B. Valdez Salas, M. Schorr Wiener, R. Zlatev Koytchev, G. López Badilla, R. Ramos Irigoyen, M. Carrillo Beltrán, N. Radnev Nedev, M. Curiel Alvarez, N. Rosas Gonzalez, J.M. Bastidas Rull, Copper corrosion by atmospheric pollutants in the electronics industry, ISRN Corrosion 2013 (2013) 846405.

[54] T.E. Graedel, J.P. Franey, G.W. Kammlott, The corrosion of copper by atmospheric sulphurous gases, Corros. Sci. 23 (11) (1983) 1141–1152.

[55] D. Li, Y. Mei, Y. Xin, Z. Li, P.K. Chu, C. Ma, G.Q. Lu, Reducing migration of sintered ag for power devices operating at high temperature, IEEE Trans. Power Electron. 35 (12) (2020) 12646–12650.

[56] S. Plimpton, Fast Parallel Algorithms for Short-Range Molecular Dynamics, J. Comput. Phys. 117 (1) (1995) 1–19.

[57] A. Stukowski, Visualization and analysis of atomistic simulation data with OVITO–the open visualization tool, Model. Simul. Mater. Sci. Eng. 18 (1) (2010) 015012.

[58] S.M. Foiles, M.I. Baskes, M.S. Daw, Embedded-atom-method functions for the fcc metals Cu, Ag, Au, Ni, Pd, Pt, and their alloys, Phys. Rev. B 33 (12) (1986) 7983–7991.

[59] M.S. Daw, S.M. Foiles, M.I. Baskes, The embedded-atom method: a review of theory and applications, Mater. Sci. Rep. 9 (7) (1993) 251–310.

[60] A.C.T. van Duin, S. Dasgupta, F. Lorant, W.A. Goddard, ReaxFF: A Reactive Force Field for Hydrocarbons, Chem. A Eur. J. 105 (41) (2001) 9396–9409.

[61] D. Wang, Y.-H. Mei, H. Xie, K. Zhang, K.S. Siow, X. Li, G.-Q. Lu, Roles of palladium particles in enhancing the electrochemical migration resistance of sintered nano-silver paste as a bonding material, Mater. Lett. 206 (2017) 1–4.